Research Square

Preprints are preliminary reports that have not undergone peer review.
They should not be considered conclusive, used to inform clinical practice,
or referenced by the media as validated information.

Turbophoresis of inertial particles in inhomogeneous turbulence generated by oscillating grids

Elad Elmakies
The Ben-Gurion University of the Negev
Oleg Shildkrot
The Ben-Gurion University of the Negev
Nathan Kleeorin
The Ben-Gurion University of the Negev
Avi Levy
The Ben-Gurion University of the Negev
Igor Rogachevskii
gary@bgu.ac.il

The Ben-Gurion University of the Negev

Research Article

Keywords: Experiments in inhomogeneous oscillating grid turbulence, Turbophoresis of inertial particles, Particle Image Velocimetry and Image Processing techniques

Posted Date: September 29th, 2026

DOI: https://doi.org/10.21203/rs.3.rs-10405586/v1

License: This work is licensed under a Creative Commons Attribution 4.0 International License.
Read Full License

Additional Declarations: No competing interests reported.

Turbophoresis of inertial particles in inhomogeneous turbulence generated by oscillating grids

Elad Elmakies, Oleg Shildkrot, Nathan Kleeorin, Avi Levy, Igor Rogachevskii

The Pearlstone Center for Aeronautical Engineering Studies, Department of Mechanical Engineering, The Ben-Gurion University of the Negev, POB 653, Beer-Sheva 8410530, Israel.

Contributing authors: eladelm@post.bgu.ac.il; olegshil@post.bgu.ac.il; nat@bgu.ac.il; avi@bgu.ac.il; gary@bgu.ac.il;

Abstract

Turbophoresis in inhomogeneous turbulent flows leads to the formation of large-scale nonuniform particle number density distributions of inertial particles. This effect is associated with an effective drift velocity directed toward regions of lower turbulence intensity. It depends on the Stokes and Reynolds numbers, as well as on the gradient of the turbulence intensity. In the present study, turbophoretic transport is experimentally investigated in air turbulent flows generated by one-grid and two-grid oscillating systems. The flow velocity field is measured using Particle Image Velocimetry, and the particle spatial distribution is obtained by applying image processing techniques. To isolate the effect of particle accumulation due to turbophoresis from that associated with mean fluid flow, the measured particle number density of inertial particles is normalized by the corresponding distribution obtained for noninertial tracer particles under identical flow conditions. The measurements show preferential accumulation of inertial particles in regions of minimum mean-square turbulent velocity, consistent with the expected behavior of turbophoretic transport.

Keywords: Experiments in inhomogeneous oscillating grid turbulence, Turbophoresis of inertial particles, Particle Image Velocimetry and Image Processing techniques

1 Introduction

Transport of particles in turbulent flows has been studied extensively through theoretical analysis, laboratory and field experiments, and numerical simulations; see, e.g., Refs. [1–14]. Nevertheless, several important aspects of particle transport in turbulence remain unresolved, especially in geophysical and astrophysical flows, where the governing parameters are difficult to reproduce experimentally or numerically.

A central problem in turbulent transport of inertial particles is the formation of large-scale inhomogeneous particle number density distributions at scales exceeding the integral turbulence scale. Two turbulence-related mechanisms can lead to such particle accumulation. The first mechanism is turbulent thermal diffusion in temperature-stratified turbulence, which causes inertial and noninertial particles to accumulate near regions of minimum mean fluid temperature [15, 16]. The second mechanism is turbophoresis, where inertial particles migrate toward regions of lower turbulence intensity in spatially inhomogeneous turbulent flows [17, 18].

Turbulent thermal diffusion produces an additional nondiffusive turbulent flux of particles $\boldsymbol{J}_{\rm TTD} = \overline{n}\,\boldsymbol{V}_{\rm TTD}$ [14–16], where $\boldsymbol{V}_{\rm TTD} = -\alpha\,D_{\rm T}\,\boldsymbol{\nabla}\ln\overline{T}$ is the effective drift velocity in a temperature-stratified turbulence, $\overline{n}$ is the mean particle number density, $\overline{T}$ is the mean fluid temperature, $D_{\rm T}$ is the turbulent diffusion coefficient, and the parameter α depends on the Stokes and Reynolds numbers for inertial particles, while $\alpha = 1$ for noninertial particles. Turbulent thermal diffusion has been investigated theoretically [14–16, 19–24], numerically [25, 26], in laboratory experiments [27–35] as well as in geophysical, planetary and astrophysical turbulence applications [36–39].

Turbophoresis is due to the joint effect of particle inertia and spatial inhomogeneity of turbulence. In the present study, we investigate turbophoresis of inertial particles in laboratory experiments. The equation of motion for inertial particles with the material density $\rho_{\rm p}$ that is much larger than the fluid density ρ, is given by

$$\frac{{\rm d}\boldsymbol{U}^{({\rm p})}}{{\rm d}t} = -\frac{\boldsymbol{U}^{({\rm p})} - \boldsymbol{U}}{\tau_p} + \boldsymbol{g}, \tag{1}$$

where $\boldsymbol{U}^{({\rm p})}$ is the particle velocity, $\boldsymbol{U}$ is the fluid velocity, $\boldsymbol{g}$ is the acceleration caused by the gravity field, and $\tau_{\rm p} = m_{\rm p}/(3\pi\rho\,\nu\,d_{\rm p})$ is the Stokes time of spherical solid particles having the diameter $d_{\rm p}$ and mass $m_{\rm p} = (\pi/6)\,\rho_{\rm p}\,d_{\rm p}^3$, and ν is the kinematic viscosity of the fluid. Turbophoresis originates from averaging of particle velocity. In particular, the mean particle velocity $\overline{\boldsymbol{U}}^{({\rm p})}$ is given by $\overline{\boldsymbol{U}}^{({\rm p})} = \overline{\boldsymbol{U}} + \overline{\boldsymbol{V}}_{\rm turboph} + \boldsymbol{V}_{\rm g}$ [17, 18], where $\overline{\boldsymbol{U}}$ is the mean fluid velocity, $\boldsymbol{V}_{\rm g} = \tau_{\rm p}\,\boldsymbol{g}$ is the terminal fall velocity of inertial particles in the gravity field, and

$$\overline{\boldsymbol{V}}_{\rm turboph} = -\kappa_{\rm turboph}\,\boldsymbol{\nabla}\left\langle \boldsymbol{u}^2 \right\rangle \tag{2}$$

is the turbophoretic velocity of inertial particles in an inhomogeneous turbulence, and $\kappa_{\rm turboph}$ is the turbophoretic coefficient, which depends on the Stokes and Reynolds numbers. Here the quantities with overline denote mean fields and the angular brackets imply ensemble averaging. The parameter $\kappa_{\rm turboph}$ vanishes for noninertial particles, so that turbophoretic transport occurs only for inertial particles.

The physical mechanism underlying turbophoresis is associated with particle inertia in spatially inhomogeneous turbulence. Due to centrifugal effects, inertial particles cannot fully follow fluid turbulent motions and tend to drift out to the regions between turbulent eddies where fluid velocity fluctuations vanish and fluid pressure fluctuations are maximum. In homogeneous and isotropic turbulence without preferred direction, this drift does not produce a net large-scale particle transport. However, in the presence of a nonzero turbulence intensity gradient, $\boldsymbol{\nabla}\left\langle \boldsymbol{u}^2 \right\rangle$, the particle drift results in a net turbophoretic flux, and inertial particles preferentially accumulate near the minimum of the turbulence intensity.

It is important to distinguish between turbulent thermal diffusion and turbophoresis, since these mechanisms originate from different physical processes. Turbulent thermal diffusion is a collective phenomenon (see, e.g., Ref. [14]), it occurs in temperature-stratified turbulence and is associated with turbulent particle flux (correlation of particle velocity and number density fluctuations) coupled to turbulent heat flux (correlation of fluid velocity and temperature fluctuations). In contrast, turbophoresis originates from averaging of particle velocity [17, 18], and it is due to particle inertia in spatially inhomogeneous turbulence, leading to preferential accumulation of particles in regions of lower turbulence intensity.

Turbophoresis has been studied extensively using analytical and numerical approaches in different types of turbulent flows [17, 18, 40–49]. Direct numerical simulations (DNS) demonstrate that inertial particles in inhomogeneously forced isothermal turbulence accumulate preferentially in regions of minimum mean-square turbulent velocity [46]. In these flows, the spatial distribution of inertial particles is governed by the competition between turbophoretic transport and turbulent diffusion. The DNS results also show that the product $\kappa_{\rm turboph}$ and $u_{\rm rms} \equiv \sqrt{\langle \boldsymbol{u}^2 \rangle}$ increases linearly with St for $\mathrm{St} \ll 1$, reaches a maximum near $\mathrm{St} \sim 10$, and decreases as $\mathrm{St}^{-1/3}$ for large St. Here, $\mathrm{St} = \tau_{\rm p}/\tau_0$ is the Stokes number defined as a ratio of the Stokes time $\tau_{\rm p}$ and the characteristic turbulent time scale τ_0 associated with the integral turbulence scale.

Numerical studies of turbophoresis in inhomogeneous turbulent Kolmogorov flows also demonstrate that the large-scale clustering of inertial particles increases at small St and gradually weakens at larger St [45]. Although these studies did not explicitly interpret the results in terms of a balance between turbophoretic and turbulent diffusive fluxes, the observed particle accumulation reflects the combined action of turbophoretic and turbulent diffusive transport. Turbophoresis may be important for various geophysical, planetary and astrophysical turbulent flows [36–39, 50].

Despite substantial progress in theoretical and numerical studies, direct experimental investigations of turbophoresis remain relatively limited, particularly in nearly unbounded turbulent flows generated away from solid boundaries. Most previous experimental studies of particle accumulation have been conducted in wall-bounded turbulent flows, where turbulence inhomogeneity is strongly affected by walls and mean shear [51–53]. The experimental identification of turbophoretic transport is therefore challenging, especially in flows where multiple particle transport mechanisms may coexist.

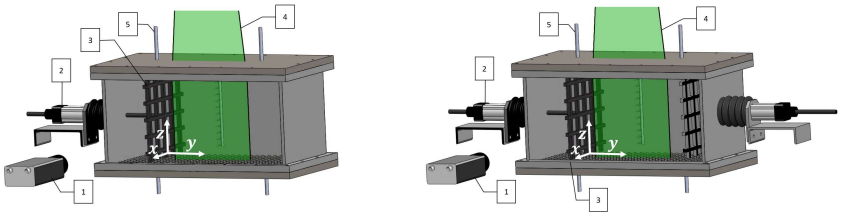


Fig. 1 Experimental setup with an isothermal turbulence produced by one oscillating grid (left panel) and by two oscillating grids (right panel): (1) digital CCD camera; (2) rod driven by the speed-controlled motor; (3) oscillating grid; (4) laser light sheet; (5) the inlets of acoustic feeding device for particle injection.

In the present study, we experimentally investigate the formation of large-scale concentrations of inertial particles in strongly inhomogeneous isothermal turbulence generated by one and two oscillating grids in air flows. Oscillating-grid turbulence provides a controlled laboratory configuration with relatively weak mean flow and spatially varying turbulence intensity, allowing direct investigation of particle accumulation induced by turbophoresis. Simultaneous measurements of turbulent velocity fields and particle number density distributions allow direct comparison between the spatial distribution of inertial particles and the turbulence intensity. To isolate the turbophoretic contribution, the measured particle number density fields for inertial particles are normalized using corresponding measurements obtained with noninertial particles under identical flow conditions.

The goal of this paper is to provide direct laboratory evidence of large-scale accumulation of inertial particles in oscillating-grid turbulence and to test whether the measured inertial-particle distribution follows the expected spatial trend relative to the turbulence-intensity field known from analytical and numerical study of turbophoresis. The robustness of this trend is examined in two distinct turbulent-flow configurations generated by one oscillating grid and by two oscillating grids. These configurations differ in the spatial structure of turbulence intensity, anisotropy, integral length scales, characteristic turbulent time, and Reynolds-number distribution. The experiments show that in both turbulent-flow configurations, inertial particles preferentially accumulate in regions of lower turbulence intensity.

This paper is organized as follows. Section 2 describes the experimental setup and measurement techniques, and Section 3 analyzes the experimental results. Finally, Section 4 outlines the conclusions.

2 Experimental setup and measurement technique

Experiments on turbophoresis of inertial particles are performed in isothermal inhomogeneous turbulence generated by one and two oscillating grids in air flows. The experiments were conducted in a rectangular transparent chamber with dimensions $L_x \times L_y \times L_z$, where $L_x = L_z = 26$ cm and $L_y = 53$ cm. The Z axis is vertical, while the Y axis is perpendicular to the grid plane (see Fig. 1).

Each oscillating grid has dimensions of 25×25 cm^2 and consists of a square array of bars with a mesh size of 5 cm and a bar width of 1 cm. The grids are positioned in

the XZ plane, parallel to the chamber side walls at a distance of 10 cm, corresponding to two grid meshes from the side walls of the chamber. The grids oscillate along the Y direction with frequency $f = 10.5$ Hz and stroke amplitude $A_g = 6$ cm. The grid Reynolds number based on the grid mesh size $M = 5$ cm is $\mathrm{Re_M} = fM^2/\nu = 1750$.

The laser light sheet is located in the central vertical YZ plane at $X = 0$. Thus, the velocity and particle-number-density measurements are performed in the central optical plane of the chamber. The grids drive the carrier flow and generate the inhomogeneous turbulence. The inertial particles are not injected directly onto the grids, and the analyzed particle-number-density fields are obtained away from the immediate vicinity of the grid bars. Therefore, the measured large-scale particle distributions are interpreted as resulting from transport by the turbulent carrier flow rather than from direct mechanical interaction with the oscillating grids.

Each grid performs an approximately sinusoidal translational motion normal to the grid plane. The motion is described as simple harmonic motion. In the double-grid configuration, the two grids are driven by separate motors. They are operated at the same nominal frequency and stroke amplitude, but they are not mechanically or electronically connected. Therefore, no fixed phase difference between the two grids is prescribed during the measurements. The relative phase is not controlled and is allowed to vary during the acquisition. The values of the frequency and amplitude are chosen as fixed operating conditions that provide sufficiently strong and reproducible turbulence in the measurement region, while maintaining stable grid motion, adequate optical access, and reliable velocity and particle-number-density measurements.

Rectangular pins of size $3 \times 3 \times 15$ mm are mounted on the upper and lower walls of the chamber (see Fig. 1) to reduce the mean flow velocity in the core region and to enhance the spatial inhomogeneity of the mean flow. The rectangular pins are passive flow-modifying elements. They do not generate the turbulence that is produced by the oscillating grids. Their role is to disturb the residual large-scale circulation and introduce local blockage and wake regions near the boundaries, thereby enhancing the spatial gradients of turbulence intensity in the measurement region. The resulting inhomogeneity is quantified directly from the velocity measurements.

The velocity field is measured using a Particle Image Velocimetry (PIV) system [54–56] consisting of a Nd-YAG laser (Continuum Surelite, 2×170 mJ) with a wavelength of 532 nm and a 12-bit CCD camera. The velocity fields are measured in a flow domain of 209.1×155.4 mm^2 using images with a resolution of 1376×1024 pixels, corresponding to a spatial resolution of 151 μm/pixel. The velocity field in the probed region is analyzed using interrogation windows of 16×16 pixels with 25 % overlap, and the pulse separation is $\Delta t = 1500\,\mu$s.

The laser provides a single-pulse energy of 170 mJ. The PIV image pairs are acquired at the rate 2 Hz, and the laser is externally triggered at the same pulse-pair acquisition rate. The acquisition is not synchronized with the oscillating grid motion, whose frequency is 10.5 Hz. The velocity statistics are obtained from 530 image pairs acquired over many grid-oscillation cycles rather than at a fixed phase of the grid motion.

Incense smoke with solid spherical particles is used as a tracer for the PIV measurements. The particles have a mean diameter of 0.7 μm and a material density $\rho_\mathrm{p} \approx 10^3\overline{\rho}$,

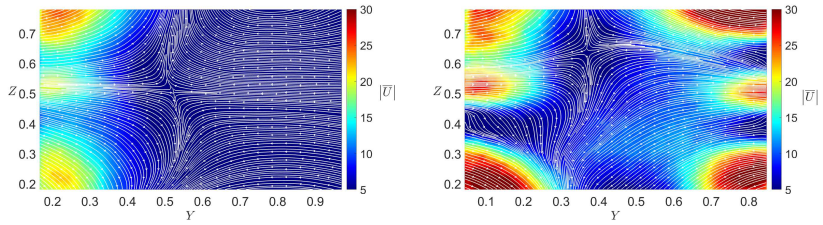


Fig. 2 Spatial distributions of the mean velocity field $\overline{U}$ in the YZ plane for turbulence generated by one oscillating grid (left panel) and two oscillating grids (right panel). The velocity is measured in cm. The coordinates Y and Z are normalized by $L_z = 26$ cm.

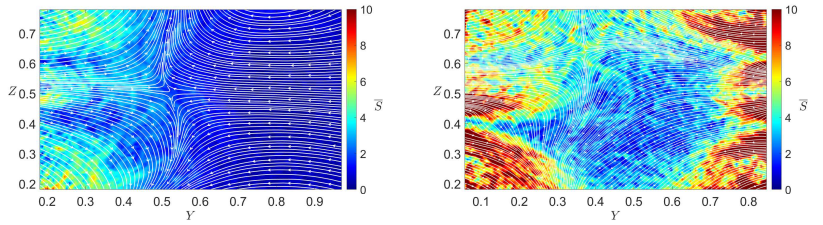


Fig. 3 Spatial distributions of the mean velocity shear $\overline{S} = \left[(\nabla_y \overline{U}_y)^2 + (\nabla_z \overline{U}_y)^2 + (\nabla_y \overline{U}_z)^2 + (\nabla_z \overline{U}_z)^2\right]^{1/2}$ in the YZ plane for turbulence generated by one oscillating grid (left panel) and two oscillating grids (right panel). Streamlines (white) of the mean velocity field $\overline{\boldsymbol{U}}$ are superimposed on the distributions. The coordinates Y and Z are normalized by $L_z = 26$ cm, and the mean velocity shear $\overline{S}$ is measured in s^{-1}.

where $\overline{\rho} = 10^{-3}$ g cm^{-3} is the mean fluid density. The particles are generated by high-temperature sublimation of solid incense grains (see Ref. [31] for details).

Using the velocity measurements, we determine various mean-flow (Figs. 2–3) and turbulent (Figs. 4–11) characteristics; see Sec. 3 for details. In particular, the mean velocity field, mean velocity shear, root-mean-square (r.m.s.) velocities, turbulent anisotropy parameter, two-point velocity correlation functions and integral turbulence length scales are obtained. The mean and r.m.s. velocity fields are determined at each spatial location by averaging over 530 independent velocity maps.

The mean velocity and rms velocity profiles are also recalculated using subsets of the recorded data, and they are compared with the final profiles obtained from all 530 velocity maps. The profiles obtained from the later subsets and from the full data set showed only small variations, indicating that the statistical estimates are stable with respect to the number of velocity maps used in the averaging. The profiles changed only very weakly when the number of velocity maps included in the averaging is varied.

The consecutive velocity maps are separated by 0.5 s (since they are acquired at the rate 2 Hz). This timescale is much larger than the characteristic turbulent correlation time in the measurement region. Therefore, the velocity maps used in the averaging can be treated as statistically independent for the purpose of estimating the mean and rms velocity fields. In addition, the size of the probed region does not affect the obtained results.

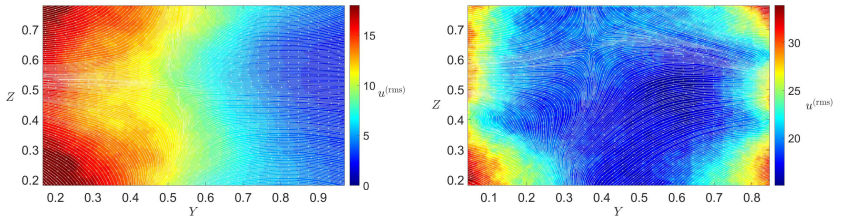


Fig. 4 Spatial distributions of the turbulent velocity $u^{(\mathrm{rms})} = \left[\langle u_y^2\rangle + \langle u_z^2\rangle\right]^{1/2}$ in the YZ plane for turbulence generated by one oscillating grid (left panel) and two oscillating grids (right panel). Streamlines (white) of the mean velocity field $\overline{\boldsymbol{U}}$ are superimposed on the distributions. The turbulent velocity is measured in cm/s, and the coordinates Y and Z are normalized by $L_z = 26$ cm.

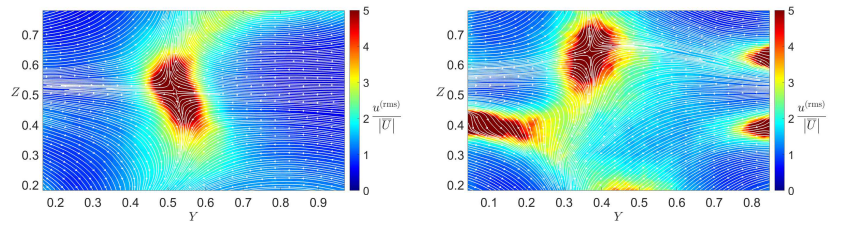


Fig. 5 Spatial distributions of the ratio $u^{(\mathrm{rms})}/|\overline{\boldsymbol{U}}|$ in the YZ plane for turbulence generated by one oscillating grid (left panel) and two oscillating grids (right panel). Streamlines (white) of the mean velocity field $\overline{\boldsymbol{U}}$ are superimposed on the distributions. The coordinates Y and Z are normalized by $L_z = 26$ cm.

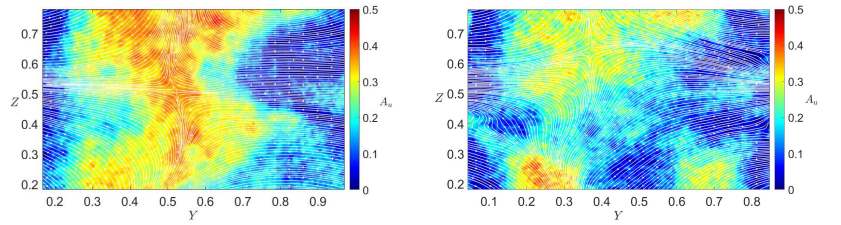


Fig. 6 Spatial distributions of the anisotropy of turbulent velocity field $A_u = |u_z^{(\mathrm{rms})}/u_y^{(\mathrm{rms})} - 1|$ in the YZ plane for a turbulence produced by one oscillating grid (left panel) and by two oscillating grids (right panel). The streamlines (white) of the mean velocity $\overline{\boldsymbol{U}}$ are also superimposed on this distribution. The coordinates Y and Z are normalized by $L_z = 26$ cm.

The integral length scales of the turbulence ℓ_y and ℓ_z in the horizontal Y and vertical Z directions are determined from two-point velocity correlation functions. Two standard approaches are applied and yield similar results. In the first approach, the normalized two-point correlation function of the velocity fluctuations is integrated over the separation distance r up to the point where the correlation decays to zero. In the second approach, the integral length scale is determined from an exponential fit of the form $\exp(-r^2/\ell_0^2)$ to the normalized correlation function.

For experimental study of turbophoresis, borosilicate hollow glass particles with an approximately spherical shape are used as inertial particles. The particles have

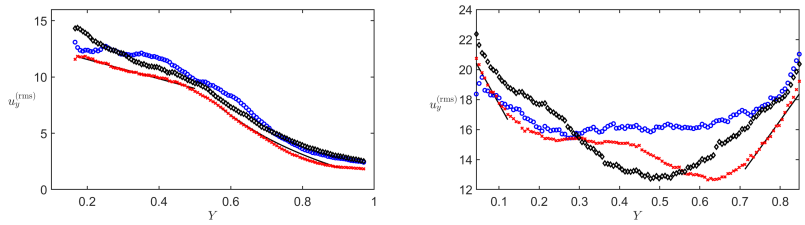


Fig. 7 The horizontal turbulent velocity $u_y^{(\mathrm{rms})}(Y)$ versus the horizontal coordinate Y in the core flow averaged over different ranges of Z for turbulence generated by one oscillating grid (left panel) and two oscillating grids (right panel). Solid lines show the fitting curves. In the left panel, the averaging is performed over $Z = 5.2$–9.3 cm (blue circles), 9.2–14.3 cm (red crosses), and 14.3–18.6 cm (black diamonds). In the right panel, the averaging is performed over $Z = 5.3$–9.4 cm (blue circles), 9.4–14.2 cm (red crosses), and 14.2–18.4 cm (black diamonds). The velocity is measured in cm/s, and the coordinate Y is normalized by $L_z = 26$ cm.

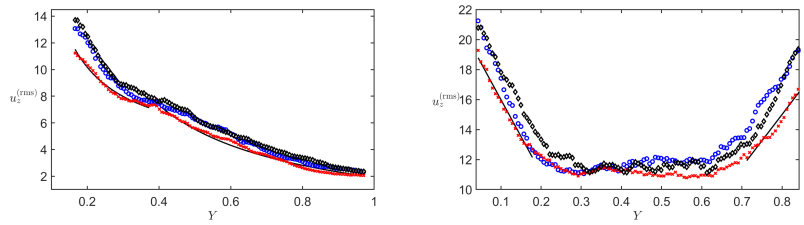


Fig. 8 The vertical turbulent velocity $u_z^{(\mathrm{rms})}(Y)$ versus the horizontal coordinate Y in the core flow averaged over different ranges of Z for turbulence generated by one oscillating grid (left panel) and two oscillating grids (right panel). Solid lines show the fitting curves. In the left panel, the averaging is performed over $Z = 5.2$–9.3 cm (blue circles), 9.2–14.3 cm (red crosses), and 14.3–18.6 cm (black diamonds). In the right panel, the averaging is performed over $Z = 5.3$–9.4 cm (blue circles), 9.4–14.2 cm (red crosses), and 14.2–18.4 cm (black diamonds). The velocity is measured in cm/s, and the coordinate Y is normalized by $L_z = 26$ cm.

a mean diameter of $10\,\mu$m and a material density of $\rho_p \approx 1.4$ g/cm^3. The inertial particles do not affect the fluid flow because the mass-loading parameter is small ($m_{\mathrm{p}} n/\rho \ll 1$). In the experiments with inertial particles, the Stokes number $\mathrm{St} = \tau_{\mathrm{p}}/\tau_0$ based on the Stokes time τ_{p} and the characteristic turbulent time scale τ_0 associated with the integral turbulence scale varies from 6.7×10^{-3} to 10.4×10^{-3} for turbulence produced by one oscillating grid, and it varies from 10.2×10^{-3} to 15.7×10^{-3} for turbulence produced by two oscillating grids. On the other hand, the Stokes number St for noninertial particles having the diameter 0.7 μm, is about 3.6×10^{-5} for the one-grid configuration and 5.5×10^{-5} for the two-grid configuration.

To improve particle mixing and reduce particle agglomeration, a custom-made acoustic feeding device is used for particle injection into the flow. The device consists of an acrylic chamber equipped with air guides and an acoustically driven flexible membrane that disperses particles into the incoming airflow. To achieve approximately uniform particle dispersion within the flow domain, the particles are injected into the chamber through two inlets located on the upper wall and two inlets positioned on the lower wall of the chamber (see Fig. 1). The inlets are small tubes used only to introduce particles into the chamber. They are not turbulence-generating elements.

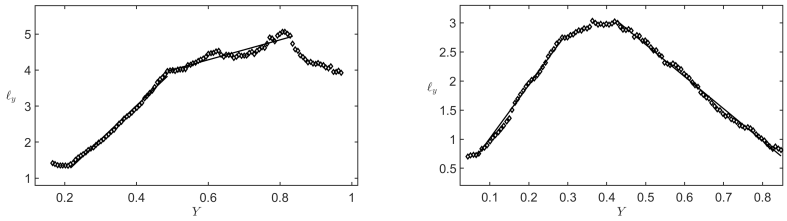


Fig. 9 The horizontal integral turbulence scale $\ell_y(Y)$ versus the horizontal coordinate Y in the core flow averaged over Z for turbulence generated by one oscillating grid (left panel) and two oscillating grids (right panel). Solid lines show the fitting curves. The integral turbulence scale is measured in cm, and the coordinate Y is normalized by $L_z = 26$ cm.

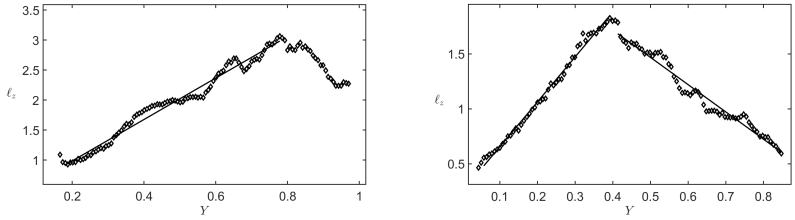


Fig. 10 The vertical integral turbulence scale $\ell_z(Y)$ versus the horizontal coordinate Y in the core flow averaged over Z for turbulence generated by one oscillating grid (left panel) and two oscillating grids (right panel). Solid lines show the fitting curves. The integral turbulence scale is measured in cm, and the coordinate Y is normalized by $L_z = 26$ cm.

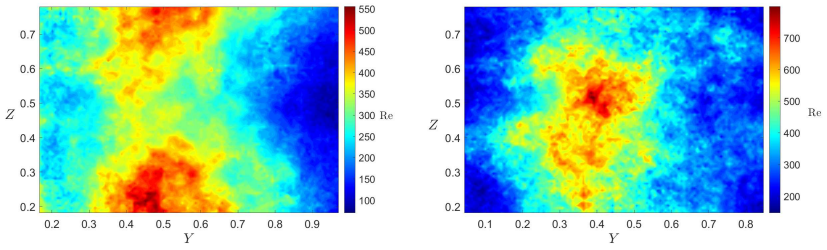


Fig. 11 Spatial distributions of the Reynolds number $\mathrm{Re} = [u_y^{(\mathrm{rms})}\,\ell_y + 2u_z^{(\mathrm{rms})}\,\ell_z]/\nu$ in the YZ plane for turbulence generated by one oscillating grid (left panel) and two oscillating grids (right panel). The coordinates Y and Z are normalized by $L_z = 26$ cm.

Their diameter is small compared with the chamber height, and they are located near the walls, away from the central optical measurement region. The measurements are performed after the injected particles are dispersed in the chamber, so that the analyzed particle-number-density fields do not represent the immediate inlet region.

The spatial distributions of particles with diameters of $0.7\,\mu$m and $10\,\mu$m are obtained in separate experiments using Mie light scattering measurements [57]. The mean scattered-light intensity is determined using interrogation windows of 32×32 pixels with 50% overlap. For turbulence generated by one oscillating grid, the measurements are performed on a grid of 85×64 interrogation windows, while for turbulence

generated by two oscillating grids the measurements are performed on a grid of 65×51 interrogation windows. This procedure enables determination of the vertical distributions of scattered-light intensity in vertical strips composed of interrogation windows.

The scattered-light intensity produced by small particles is determined by Mie scattering [58]. The scattered radiation energy flux E_s depends on the particle diameter d_p, the wavelength λ, and the refractive index through the scattering function $\Psi(\pi d_\mathrm{p}/\lambda; a_0, n)$. For $\lambda \gtrsim \pi d_p$, the scattering function follows the Rayleigh scattering regime and depends on particle diameter, whereas for $\lambda \lesssim \pi d_p$ the scattering function becomes weakly dependent on both particle diameter and wavelength. The scattered radiation energy flux E_s is proportional to the local particle number density n. Therefore, the scattered-light intensity recorded by the CCD camera can be used to determine the spatial distributions of particle number density.

For a fixed particle type and optical configuration, the frame-averaged scattered-light intensity is proportional to the local particle number density. Therefore, the analysis is based on normalized relative particle-density fields rather than on absolute particle concentrations. To isolate turbophoretic particle accumulation from other possible transport mechanisms, the scattered-light intensity E_in measured for inertial particles is normalized pointwise by the scattered-light intensity E_nin obtained in separate experiments with noninertial particles under identical flow conditions. This normalization enables characterization of the spatial distribution of particle number density associated with turbophoretic transport.

The reliability of the measurements is assessed by considering the main sources of uncertainty associated with the velocity and particle number density fields. The velocity field is measured using the PIV system, and its quality is evaluated using the standard Q-factor criterion, defined as the ratio between the primary and secondary peaks of the cross-correlation function [54–56]. The spatially averaged Q factor is approximately 1.6 or higher throughout the data set, indicating reliable cross-correlation and sufficient signal-to-noise ratio for accurate velocity measurements. Standard validation procedures are applied to remove spurious vectors and ensure robustness of the velocity field.

The particle number density is determined from the ratio of frame-averaged scattered-light intensities measured for inertial and noninertial particles. The corresponding uncertainty is evaluated using first-order error propagation (the δ method), accounting for the independent contributions of both measurements [59], and varies from 4% to 8% with 95% confidence interval. Overall, the uncertainties in the velocity and particle number density measurements remain small relative to the observed flow variations and do not affect the main conclusions of the study.

The experimental methodology and data-processing procedures employed in the present study are based on approaches previously developed for investigations of turbulent convection [32, 33, 35, 60–62], stably stratified turbulence [31, 63, 64], turbulent thermal diffusion [24, 27–29], particle mixing in inhomogeneous turbulence [31, 33, 65], and small-scale particle clustering [66].

3 Experimental results

This section presents the experimental results on large-scale inhomogeneous distributions of inertial particles in turbulence generated by one and two oscillating grids in airflow (see Fig. 1). The main objective is to investigate turbophoretic transport of inertial particles in strongly inhomogeneous turbulence at sufficiently large Reynolds numbers. Therefore, the turbulence characteristics are analyzed primarily to characterize the flow inhomogeneity responsible for turbophoretic transport, while the main focus is placed on the spatial distributions and accumulation of inertial particles.

Figure 2 shows the spatial distributions of the mean velocity field $\overline{\boldsymbol{U}}$ in the YZ plane for inhomogeneous isothermal turbulence generated by one oscillating grid (left panel) and two oscillating grids (right panel). The mean velocity field produced by two oscillating grids is nearly symmetric with respect to the Y axis. The large-scale velocity shear

$$\overline{S} = \left[(\nabla_y \overline{U}_y)^2 + (\nabla_z \overline{U}_y)^2 + (\nabla_y \overline{U}_z)^2 + (\nabla_z \overline{U}_z)^2\right]^{1/2}$$

is stronger near the oscillating grids (see Fig. 3). The maximum dimensionless shear parameter is approximately $\overline{S}^{(\max)}\tau_0 \approx 0.3$ for turbulence generated by one oscillating grid, where the characteristic turbulent time is $\tau_0 \approx 0.05$ s, and $\overline{S}^{(\max)}\tau_0 \sim 0.4$ for turbulence generated by two oscillating grids, where $\tau_0 \approx 0.033$ s.

Figures 4–11 present the following turbulent characteristics in the YZ plane:

- the turbulent velocity $u^{(\mathrm{rms})} = \left[\langle u_y^2\rangle + \langle u_z^2\rangle\right]^{1/2}$ (see Fig. 4);
- the ratio between turbulent and mean velocities $u^{(\mathrm{rms})}/|\overline{\boldsymbol{U}}|$ (see Fig. 5);
- the turbulence anisotropy parameter $A_u = |u_z^{(\mathrm{rms})}/u_y^{(\mathrm{rms})} - 1|$ (see Fig. 6);
- the horizontal profiles of the turbulent velocity components $u_y^{(\mathrm{rms})}(Y)$ and $u_z^{(\mathrm{rms})}(Y)$ (see Figs. 7–8), together with the integral turbulence length scales $\ell_y(Y)$ and $\ell_z(Y)$ (see Figs. 9–10);
- the Reynolds number based on turbulent characteristics,

$$\mathrm{Re} = \frac{1}{\nu}\left[u_y^{(\mathrm{rms})}\,\ell_y + 2u_z^{(\mathrm{rms})}\,\ell_z\right] \tag{3}$$

(see Fig. 11).

Generally, the Reynolds number is estimated as $\mathrm{Re} = \tau_0\langle \boldsymbol{u}^2\rangle/\nu$, where $\langle \boldsymbol{u}^2\rangle = \langle u_x^2\rangle + \langle u_y^2\rangle + \langle u_z^2\rangle$ and τ_0 is the characteristic turbulent time in the integral scale. The estimate (3) assumes similar turbulent time scales in the X, Y, and Z directions, $\tau_0 = \ell_x/u_x^{\mathrm{rms}} = \ell_y/u_y^{\mathrm{rms}} = \ell_z/u_z^{\mathrm{rms}}$ together with the condition $u_x^{\mathrm{rms}} \approx u_z^{\mathrm{rms}}$.

The flow in the chamber is inhomogeneous and anisotropic, so the assumption of identical turbulent time scales in all directions and the assumption of $u_x^{\mathrm{rms}} \approx u_z^{\mathrm{rms}}$ represent approximations. The PIV measurements provide two velocity components in the YZ plane, while the third velocity component along the X axis is not measured directly. Therefore, the resulting turbulent quantities should be regarded as estimates

of the corresponding flow characteristics. However, our previous studies [27, 35] have shown that these assumptions are valid for our experimental setups.

The turbulence is generated primarily by the forcing produced by the oscillating grids, and the large-scale shear also contributes to the turbulent kinetic energy. To visualize different flow regions, streamlines of the mean velocity field are superimposed on the spatial distributions of the turbulence characteristics. Velocity fluctuations are stronger near the oscillating grids, and the turbulence intensity decreases with increasing distance Y from the grids (see Figs. 4 and 7–8). The turbulent velocity field generated by two oscillating grids is more symmetric in the horizontal direction and less anisotropic than that generated by one oscillating grid (see Figs. 4 and 6). In most parts of the domain, the turbulent velocity exceeds the mean velocity (see Fig. 5). Turbulent velocity varies from 2 to 17 cm/s for turbulence produced by one oscillating grid and from 19 to 32 cm/s for turbulence produced by two oscillating grids.

The integral turbulence length scales in turbulence produced by one oscillating grid are larger than those produced by two oscillating grids (see Figs. 9–10). The measured integral scales exhibit approximately linear dependencies, $\ell_i(Y) \propto Y$, in the left and right regions of the horizontal coordinate Y. Similar scalings were reported in earlier laboratory experiments on turbulent water flows produced by one oscillating grid [67–73], where the integral turbulence length scales increased linearly with the distance from the grid.

To investigate turbophoresis of inertial particles in inhomogeneous turbulence, we measure the spatial distributions of the normalized mean particle number density. The initial spatial distribution of the injected particles is nearly homogeneous and isotropic. The normalization procedure described in Sec. 2 is used to isolate turbophoretic particle accumulation from other transport effects.

The spatial distribution of inertial particles is determined by equation for the particle number density $n(t, \boldsymbol{x})$:

$$\frac{\partial n}{\partial t} + \boldsymbol{\nabla} \cdot \left(\boldsymbol{U}^{(\mathrm{p})}\, n \right) = D\, \Delta n, \tag{4}$$

where $D = k_B\, T/(3\pi\rho\,\nu\, d_{\mathrm{p}})$ is the coefficient of the molecular (Brownian) diffusion of particles, T is the fluid temperature and k_B is the Boltzmann constant. Averaging Eq. (4) over an ensemble yields an equation for the mean particle number density $\overline{n}$:

$$\frac{\partial \overline{n}}{\partial t} + \boldsymbol{\nabla} \cdot \left[\overline{\boldsymbol{U}}^{(\mathrm{p})} \overline{n} + \langle \boldsymbol{u}^{(\mathrm{p})}\, n' \rangle \right] = D\, \Delta \overline{n}, \tag{5}$$

where $\boldsymbol{u}^{(\mathrm{p})}$ are fluctuations of particle velocity and n' are particle number density fluctuations. Mean-field equation for particle number density similar to Eq. (5), has been derived by means of various analytical approaches (see, e.g., Refs. [5, 11, 14]).

For large Péclet numbers, the molecular Brownian diffusion coefficient D can be neglected, because it is much smaller than turbulent diffusion coefficient. In Eq. (5), we use equation for the mean particle velocity $\overline{\boldsymbol{U}}^{(\mathrm{p})} = \overline{\boldsymbol{U}} + \tau_{\mathrm{p}}\, \boldsymbol{g} - \kappa_{\mathrm{turboph}}\, \boldsymbol{\nabla} \langle \boldsymbol{u}^2 \rangle$ and take into account that the turbulent flux of particles $\langle u_i^{(\mathrm{p})}\, n' \rangle$ in an anisotropic

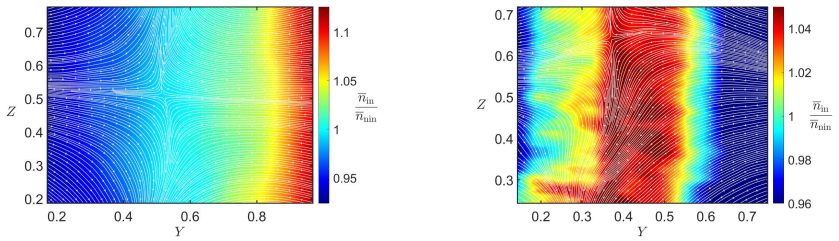


Fig. 12 Spatial distributions of the normalized mean particle number density $\overline{n}_{\rm in}/\overline{n}_{\rm nin}$ in the YZ plane for turbulence generated by one oscillating grid (left panel) and two oscillating grids (right panel). Streamlines (white) of the mean velocity field $\overline{U}$ are superimposed on the particle distributions. The coordinates Y and Z are normalized by $L_z = 26$ cm.

turbulence is given by $\langle u_i^{(\rm p)}\, n' \rangle = \langle u_i\, n' \rangle + {\rm O}(\tau_{\rm p}/\tau_0) = -D_{ij}^{(\rm T)} \nabla_j \overline{n}$, where τ_0 is the characteristic turbulent time scale associated with the integral turbulence scale and $D_{ij}^{(\rm T)}$ is the turbulent diffusion tensor. In the turbulent flux of particles we neglect small effects $\sim {\rm O}(\tau_{\rm p}/\tau_0)$.

For simplicity, we assume that gradients of $\langle \boldsymbol{u}^2 \rangle$ and $\overline{n}$ along the horizontal direction (e.g., along the Y axis) dominate over gradients in the remaining directions, consistent with the experimental conditions considered in the present study. The steady-state solution (5) at a zero total particle flux at the boundaries is given by

$$\frac{\overline{n}(Y)}{\overline{n}_{\rm b}} = \exp\!\left(\int_0^Y \frac{\overline{U}_y - \kappa_{\rm turboph}\, \nabla_y \langle \boldsymbol{u}^2 \rangle}{D_{yy}^{(\rm T)}}\, {\rm d}Y' \right), \tag{6}$$

where $D_{yy}^{(\rm T)} = \ell_y \left[\langle u_y^2 \rangle \right]^{1/2}$ is the horizontal component of the turbulent diffusion tensor, ℓ_y is the integral scale along the Y axis and $\overline{n}_{\rm b} = \overline{n}(Y=0)$. Using the steady-state solution for the mean particle number density given by Eq. (6), we obtain the ratio of the mean number densities of inertial particles, $\overline{n}_{\rm in}$, and noninertial particles, $\overline{n}_{\rm nin}$, for identical flow conditions:

$$\frac{\overline{n}_{\rm in}(Y)}{\overline{n}_{\rm nin}} \approx \left(\frac{\langle \boldsymbol{u}^2 \rangle\,(Y)}{\langle \boldsymbol{u}^2 \rangle_{\rm max}} \right)^{-\frac{a_* \kappa_{\rm turboph}}{\tau_0}}, \tag{7}$$

where $\langle \boldsymbol{u}^2 \rangle_{\rm max}$ is the maximum turbulence intensity in the flow domain, and a_* is a coefficient that depends on turbulence anisotropy (e.g., $a_* = 3$ for isotropic turbulence and $a_* > 3$ for anisotropic turbulence). Equation (7) is derived assuming that the parameters $\kappa_{\rm turboph}$ and τ_0 vary weakly along the horizontal coordinate Y.

Figure 12 shows the spatial distributions of the normalized mean particle number density $\overline{n}_{\rm in}/\overline{n}_{\rm nin}$ in the YZ plane. To analyze turbophoretic particle accumulation, we plot in Fig. 13 the Y-dependencies of the normalized turbulence intensity $\langle \boldsymbol{u}^2 \rangle / \langle \boldsymbol{u}^2 \rangle_{\rm max}$, and the normalized mean particle number density $\overline{n}_{\rm in}/\overline{n}_{\rm nin}$ for turbulence produced by one oscillating grid (left panel) and two oscillating grids (right panel). Here the turbulence intensity $\langle \boldsymbol{u}^2 \rangle$ is normalised by its maximum value

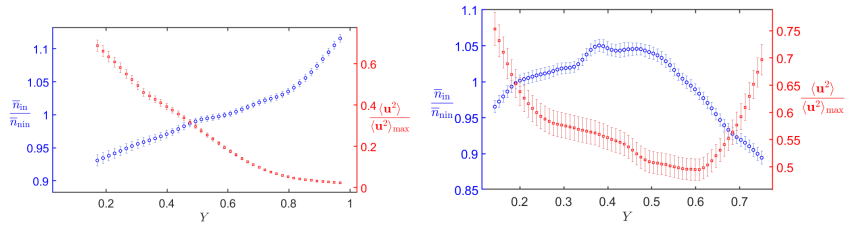


Fig. 13 The Y-dependences of the normalized turbulence intensity $\langle \boldsymbol{u}^2 \rangle / \langle \boldsymbol{u}^2 \rangle_{\max}$ (red) and the normalized mean particle number density $\overline{n}_{\text{in}}/\overline{n}_{\text{nin}}$ (blue) for turbulence generated by one oscillating grid (left panel) and two oscillating grids (right panel). The coordinate Y is normalized by $L_z = 26$ cm. The error bars indicate propagated 95 % statistical confidence intervals.

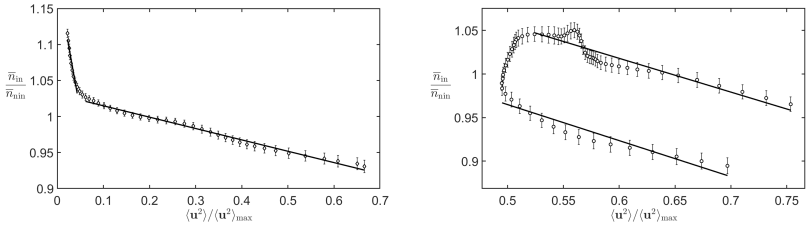


Fig. 14 The normalized mean particle number density $\overline{n}_{\text{in}}/\overline{n}_{\text{nin}}$ versus the normalized turbulence intensity $\langle \boldsymbol{u}^2 \rangle / \langle \boldsymbol{u}^2 \rangle_{\max}$ for turbulence generated by one oscillating grid (left panel) and two oscillating grids (right panel), where $\langle \boldsymbol{u}^2 \rangle_{\max}$ is the maximum turbulence intensity in the flow domain. The error bars indicate propagated 95 % statistical confidence intervals of the normalized particle-number-density.

$\langle \boldsymbol{u}^2 \rangle_{\max}$. Figures 12–13 demonstrate that inertial particles preferentially accumulate in regions of lower turbulence intensity.

To compare the experimental results with the theoretical dependence given by Eq. (7), Fig. 14 shows the normalized mean particle number density $\overline{n}_{\text{in}}/\overline{n}_{\text{nin}}$ as a function of the normalized turbulence intensity $\langle \boldsymbol{u}^2 \rangle / \langle \boldsymbol{u}^2 \rangle_{\max}$. The spatial distribution of noninertial particles remains nearly uniform throughout the domain, whereas inertial particles preferentially accumulate in regions of lower turbulence intensity. As a result, the ratio $\overline{n}_{\text{in}}/\overline{n}_{\text{nin}}$ is smaller than 1 in most parts of the flow domain, except for the regions where inertial particles are accumulated. These regions are located near the minima of the normalized turbulence intensity $\langle \boldsymbol{u}^2 \rangle / \langle \boldsymbol{u}^2 \rangle_{\max}$ (see Fig. 14). This result is consistent with the theoretical estimate given by Eq. (7).

In the two-grid configuration, the turbulence forcing is approximately symmetric with respect to the central region between the grids. Therefore, the Y-profiles in Fig. 14 form two spatial branches corresponding to the two sides of the measurement region. The solid lines are branchwise trend lines and are not theoretical fits. They are shown only to indicate that both branches exhibit the same qualitative trend: the normalized inertial-particle concentration increases as the normalized turbulence intensity decreases.

In Fig. 14 we determine also the slopes of the trend lines (the solid lines shown in Fig. 14) which quantify the sensitivity of the normalized inertial-particle concentration to changes in the normalized turbulence intensity. They should not be interpreted as spatial gradients directly, but rather considered as a measure of how strongly the normalized particle concentration changes when the turbulence intensity varies. For the one-grid configuration, the main branch gives a relatively moderate slope (≈ -0.15), while the localized branch at very low turbulence intensity gives a steeper slope (≈ -3.17). This indicates that the strongest change in the normalized particle concentration occurs in the region where the turbulence intensity is already low. This is consistent with the observed turbophoretic accumulation, since inertial particles preferentially accumulate in regions of reduced turbulence intensity.

For the two-grid configuration, the two branches have similar slopes (≈ -0.38 for the upper line) and (≈ -0.42 for the lower line). This supports the interpretation that the two branches do not represent separate physical mechanisms, rather than they correspond to the decay of turbulence intensity away from the two oscillating grids. Each branch represents one side of the approximately symmetric two-grid configuration, and both branches show the same qualitative trend: the normalized inertial-particle concentration increases as the turbulence intensity decreases. The small deviation from the trend at the upper branch is related to the stagnation point of the mean flow, but nevertheless it does not affect the whole trend.

The error bars shown in Figs. 13–14 indicate propagated 95 % statistical confidence intervals of the normalized particle-number-density ratio, $\overline{n}_{\mathrm{in}}/\overline{n}_{\mathrm{nin}}$. These uncertainties have been calculated directly from the data sets for inertial and noninertial particles. For each interrogation window, the standard error of the frame-averaged scattered-light intensity has been evaluated separately for the inertial and noninertial particle measurements, and the uncertainty of the ratio $\overline{n}_{\mathrm{in}}/\overline{n}_{\mathrm{nin}}$ has been obtained using first-order error propagation.

The uncertainty range of 4–8 % quoted in Sec. 2 represents a conservative estimate of the overall uncertainty of the particle-density measurement method, including possible systematic contributions associated with illumination nonuniformity, optical alignment, and normalization-related effects. We distinguish between this conservative overall estimate and the pointwise statistical confidence intervals shown in Figs. 13–14.

Although the mean fluid velocity field has strong vertical structure (see Fig. 2), these experiments have shown that the dominant effect of large-scale accumulation of inertial particles occurs in the horizontal direction. This indicates that the large-scale accumulation of inertial particles is mainly associated with the horizontal inhomogeneity of turbulence rather than solely with the mean fluid velocity.

There might be an additional mechanism of particle accumulation near the mean flow stagnation regions. However, as can be seen in Fig. 12 (left panel, corresponding to the one-grid configuration), the regions where inertial particles accumulate (at Y from $0.83L_z$ to $0.9L_z$) are located far from the regions with the mean flow stagnation point (at $Y = 0.55L_z$). As follows from Fig. 12 (right panel, corresponding to the two-grid configuration), the regions where inertial particles accumulate (at Y from $0.33L_z$ to $0.53L_z$ and all Z) are different from the regions with the mean flow stagnation points (at $Y = 0.36L_z$ and $Z = 0.65L_z$). In addition, as follows from our

experiments, the spatial distribution of inertial particles is nonuniform. This implies that the accumulation of inertial particles is primarily driven by inhomogeneous turbulence rather than by the mean flow stagnation point. The pointwise normalization of the inertial-particle number density by the corresponding noninertial-particle number density reduces common mean-flow and stagnation-related effects.

The observed particle accumulation is primarily a bulk effect due to turbophoresis caused by large-scale gradients of turbulence intensity rather than by boundary effects. This conclusion is supported by the measured spatial distributions of particle number density (see Figs. 13–14), which do not exhibit localization near the boundaries but instead follow the large-scale variations of turbulence intensity.

We do not use the present measurements to infer a quantitative value of the turbophoretic coefficient $\kappa_{\mathrm{turboph}}$. Such an estimate would require a fully three-dimensional characterization of the anisotropic inhomogeneous turbulence and an independent determination of the turbulent diffusion tensor. The comparison with previous theory and DNS is therefore made at the level of the observed spatial trend. The normalized inertial-particle concentration increases in regions of reduced turbulence intensity, consistent with the turbophoretic trend observed in DNS of inhomogeneously forced turbulence and with the general physical picture of turbophoretic transport.

Although inertial particles experience gravitational settling, its influence on the measured particle accumulation remains limited under the present experimental conditions. The terminal fall velocity for particles with diameter $10\,\mu$m is approximately 0.33 cm/s, which is substantially smaller than both the typical mean and turbulent fluid velocities. Gravitational settling acts in the vertical direction, whereas the observed accumulation trend is mainly associated with horizontal turbulence-intensity gradients.

The particle number density distributions are obtained from measurements with relatively short acquisition times and ensemble averaging over many independent realizations. As a result, the measured distributions primarily reflect turbophoretic redistribution of particles within the flow before significant gravitational settling develops. Therefore, the observed large-scale particle accumulation patterns are governed mainly by turbophoretic transport rather than by sedimentation effects.

4 Conclusions

In the present experimental study, we have investigated turbophoretic transport of inertial particles in inhomogeneous non-stratified turbulence in airflow. Turbophoresis is caused by the combined effect of particle inertia and turbulence inhomogeneity. The competition between the effective turbophoretic velocity and turbulent diffusion can lead to the formation of large-scale concentrations of inertial particles in regions of minimum turbulence intensity. In the experiments, the velocity field is measured using Particle Image Velocimetry, and the spatial distribution of inertial particles is obtained using image processing techniques. To isolate the effect of turbophoresis, the particle number density measured for inertial particles is normalized pointwise by the corresponding distribution obtained for noninertial particles under identical flow conditions.

We examine the behavior of inertial particles in two distinct turbulent-flow configurations produced by one and two oscillating grids. Measurements of the velocity field show that these flow configurations have different spatial structure of turbulence intensity, anisotropy, integral length scales, characteristic turbulent time, and Reynolds-number distributions. Within the parameter range of the present experiments, both one-grid and two-grid configurations show the same qualitative behavior: inertial particles preferentially accumulate in regions of reduced turbulence intensity, consistent with the theoretical estimate given by Eq. (7). In particular, the negative slopes of the solid trend lines shown in Fig. 14, indicate that the normalized inertial-particle concentration increases as the normalized turbulence intensity decreases. In the two-grid configuration, the two similar slopes correspond to the two spatial branches associated with the decay of turbulence intensity away from each oscillating grid. The larger apparent slope observed in the low-intensity branch of the one-grid configuration indicates a stronger local sensitivity of particle accumulation to changes in turbulence intensity in regions where the turbulence intensity is already low. The present results provide experimental evidence of large-scale turbophoretic particle accumulation in strongly inhomogeneous turbulence. A broad parametric experimental study of turbophoresis is the subject of a separate future investigation.

DATA AVAILABILITY

The data that support the findings of this study are available from the corresponding author upon reasonable request.

AUTHOR DECLARATIONS

Funding Declaration
This research did not receive funding.

Conflict of Interest
The authors have no conflicts of interest to declare that are relevant to the content of this article.

Author Contributions
Authors have contributed equally to the work.

References

[1] Monin AS, Yaglom AM (1971) Statistical Fluid Mechanics. MIT Press, Cambridge, Massachusetts, v. 1

[2] Monin AS, Yaglom AM (1975) Statistical Fluid Mechanics. MIT Press, Cambridge, Massachusetts, v. 2

[3] Csanady GT (1980) Turbulent Diffusion in the Environment. Reidel, Dordrecht

[4] McComb WD (1990) The Physics of Fluid Turbulence. Oxford Science Publ., Oxford

[5] Zeldovich YB, Ruzmaikin AA, Sokoloff DD (1990) The Almighty Chance. World Scientific Publ., Singapore

[6] Frisch U (1995) Turbulence: the Legacy of A. N. Kolmogorov. Cambridge University Press, Cambridge

[7] Blackadar AK (1997) Turbulence and Diffusion in the Atmosphere. Springer, Berlin

[8] Pope SB (2000) Turbulent Flows. Cambridge University Press, Cambridge

[9] Seinfeld JH, Pandis SN (2006) Atmospheric Chemistry and Physics. From Air Pollution to Climate Change. 2nd ed., John Wiley and Sons, NY

[10] Lesieur M (2008) Turbulence in Fluids. Springer, Dordrecht

[11] Zaichik LI, Alipchenkov VM, Sinaiski EG (2008) Particles in turbulent flows. John Wiley & Sons, NY

[12] Crowe CT, Schwarzkopf JD, Sommerfeld M, Tsuji Y (2011) Multiphase Flows with Droplets and Particles. 2nd edition, CRC Press LLC, NY

[13] Davidson PA (2013) Turbulence in Rotating, Stratified and Electrically Conducting Fluids. Cambridge University Press, Cambridge

[14] Rogachevskii I (2021) Introduction to Turbulent Transport of Particles, Temperature and Magnetic Fields. Cambridge University Press, Cambridge

[15] Elperin T, Kleeorin N, Rogachevskii I (1996) Turbulent thermal diffusion of small inertial particles. Phys. Rev. Lett. 76(2): 224-227

[16] Elperin T, Kleeorin N, Rogachevskii I (1997), Turbulent barodiffusion, turbulent thermal diffusion and large-scale instability in gases. Phys. Rev. E 55(3): 2713-2721

[17] Caporaloni M, Tampieri F, Trombetti F, Vittori O (1975) Transfer of particles in nonisotropic air turbulence. J. Atmosph. Sci. 32(3): 565-568

[18] M. Reeks (1983) The transport of discrete particle in inhomogeneous turbulence. J. Aerosol Sci. 14(6): 729-739

[19] Elperin T, Kleeorin N, Rogachevskii I (2000) Mechanisms of formation of aerosol and gaseous inhomogeneities in the turbulent atmosphere. Atmosph. Res. 53(1): 117-129

[20] Elperin T, Kleeorin N, Rogachevskii I, Sokoloff D (2000) Passive scalar transport in a random flow with a finite renewal time: Mean-field equations. Phys. Rev. E 61(3): 2617-2625

[21] Elperin T, Kleeorin N, Rogachevskii I, Sokoloff D (2001) Mean-field theory for a passive scalar advected by a turbulent velocity field with a random renewal time. Phys. Rev. E 64(2): 026304

[22] Pandya RVR, Mashayek F (2002) Turbulent thermal diffusion and barodiffusion of passive scalar and dispersed phase of particles in turbulent flows. Phys. Rev. Lett. 88(4): 044501

[23] Reeks MW (2005) On model equations for particle dispersion in inhomogeneous turbulence. Int. J. Multiph. Flow 31(1): 93-114

[24] Amir G, Bar N, Eidelman A, Elperin T, Kleeorin N, Rogachevskii I (2017) Turbulent thermal diffusion in strongly stratified turbulence: Theory and experiments. Phys. Rev. Fluids 2(6): 064605

[25] Haugen NEL, Kleeorin N, Rogachevskii I, Brandenburg A (2012) Detection of turbulent thermal diffusion of particles in numerical simulations. Phys. Fluids 24(7): 075106

[26] Rogachevskii I, Kleeorin N, Brandenburg A (2018) Compressibility in turbulent magnetohydrodynamics and passive scalar transport: mean-field theory. J. Plasma Phys. 84(5): 735840502

[27] Buchholz J, Eidelman A, Elperin T, Grünefeld G, Kleeorin N, Krein A, Rogachevskii I (2004) Experimental study of turbulent thermal diffusion in oscillating grids turbulence, Experim. Fluids 36(6): 879-887

[28] Eidelman A, Elperin T, Kleeorin N, Krein A, Rogachevskii I, Buchholz J, Grünefeld G (2004) Turbulent thermal diffusion of aerosols in geophysics and in laboratory experiments. Nonl. Proc. Geophys. 11(3): 343-350

[29] Eidelman A, Elperin T, Kleeorin N, Markovich A, Rogachevskii I (2006) Experimental detection of turbulent thermal diffusion of aerosols in non-isothermal flows. Nonl. Proc. Geophys. 13(1): 109-117

[30] Eidelman A, Elperin T, Kleeorin N, Rogachevskii I, Sapir-Katiraie I (2006), Turbulent thermal diffusion in a multi-fan turbulence generator with the imposed mean temperature gradient. Experim. Fluids 40(5): 744-752

[31] Elmakies E, Shildkrot O, Kleeorin N, Levy A, Rogachevskii I, Eidelman A (2022) Experimental study of turbulent thermal diffusion of particles in inhomogeneous and anisotropic turbulence. Phys. Fluids 34(5): 055125

[32] Shimberg I, Shriki O, Shildkrot O, Kleeorin N, Levy A, Rogachevskii I (2022) Experimental study of turbulent transport of nanoparticles in convective turbulence. Phys. Fluids 34(5): 055126.

[33] Elmakies E, Shildkrot O, Kleeorin N, Levy A, Rogachevskii I (2023) Experimental study of turbulent thermal diffusion of particles in an inhomogeneous forced convective turbulence. Phys. Fluids 35(9): 095123

[34] Zarbib E, Elmakies E, Shildkrot O, Kleeorin N, Levy A, Rogachevskii I (2025) Experimental investigation of turbulence and turbulent thermal diffusion in strongly inhomogeneous and anisotropic forced convection. Phys. Fluids 37(11): 115145

[35] Elmakies E, Shildkrot O, Kleeorin N, Levy A, Rogachevskii I (2026), Experimental study of turbulent thermal diffusion of inertial particles in a convective turbulence forced by oscillating grids, Phys. Fluids 38(6): 065129

[36] Elperin T, Kleeorin N, Podolak M, Rogachevskii I (1997) A mechanism for the formation of aerosol concentrations in the atmosphere of Titan. Planetary and Space Science 45(8): 923-929

[37] Sofiev M, Sofieva V, Elperin T, Kleeorin N, Rogachevskii I, Zilitinkevich SS (2009) Turbulent diffusion and turbulent thermal diffusion of aerosols in stratified atmospheric flows. J. Geophys. Res. 114(D18): D18209

[38] Hubbard A (2016), Turbulent thermal diffusion: a way to concentrate dust in protoplanetary discs. Monthly Notes Roy. Astron. Soc. 456(3): 3079-3089

[39] Kleeorin N, Rogachevskii I (2025) Large-scale clustering of inertial particles in a rotating, stratified and inhomogeneous turbulence. Phys. Fluids 37(6): 065152

[40] Guha A (1997) A unified Eulerian theory of turbulent deposition to smooth and rough surfaces. J. Aerosol Sci. 28(8): 1517-1537

[41] Elperin T, Kleeorin N, Rogachevskii I (1998) Formation of inhomogeneities in two-phase low-Mach-number compressible turbulent fluid flows. Int. J. Multiphase Flow 24(7): 1163-1182

[42] Marchioli C, Soldati A (2002) Mechanisms for particle transfer and segregation in a turbulent boundary layer. J. Fluid Mech. 468(10): 283-315

[43] Guha A (2008) Transport and deposition of particles in turbulent and laminar flow, Annu. Rev. Fluid Mech. 40(1): 311-341

[44] Sardina G, Schlatter P, Brandt L, Picano F, Casciola CM (2012) Wall accumulation and spatial localization in particle-laden wall flows. J. Fluid Mech. 699(4): 50-78

[45] De Lillo F, Cencini M, Musacchio S, Boffetta G (2016) Clustering and turbophoresis in a shear flow without walls. Phys. Fluids 28(3): 035104

[46] Mitra D, Haugen NEL, Rogachevskii I (2018), Turbophoresis in forced inhomogeneous turbulence, Europ. Phys. J. Plus 133(2): 35

[47] Johnson PL, Bassenne M, Moin P (2020) Turbophoresis of small inertial particles: theoretical considerations and application to wall-modelled large-eddy simulations. J. Fluid Mech. 883(1): A27

[48] Bec J, Vallée R (2024) Homogeneous turbophoresis of heavy inertial particles in turbulent flow. J. Fluid Mech. 999(11): A83

[49] Wang P, Zhou B, Zheng X (2024) Turbophoresis and preferential accumulation of inertial particles in compressible turbulent channel flow: Effect of Mach number. Phys. Rev. Fluids 9(3): 034305

[50] Rogachevskii I, Kleeorin N (2026) Alpha effect and dynamo in density-stratified turbulence with large-scale shear: Applications to protoplanetary discs and astrophysical clouds. Monthly Notes Roy. Astron. Soc. 547(2): stag289

[51] Squires KD, Eaton JK (1991) Preferential concentration of particles by turbulence. Phys. Fluids A3(5): 1169-1178

[52] Kaftory D, Hetsroni G, Banerjee S (1995) Particle behaviour in the turbulent boundary layer. I. Motion, deposition, and entrainment. Phys. Fluids 7(5): 1095-1106

[53] Righetti M, Romano GP (2004) Particle-fluid interactions in a plane near-wall turbulent flow. J. Fluid Mech. 505(4): 93-121

[54] Adrian RJ (1991) Particle-imaging techniques for experimental fluid mechanics. Annu. Rev. Fluid Mech. 23(1): 261-304

[55] Raffel M, Willert C, Werely S, Kompenhans J (2007) Particle Image Velocimetry. Springer, Berlin-Heidelberg

[56] Westerweel J (2000) Theoretical analysis of the measurement precision in particle image velocimetry. Experim. Fluids 29(Suppl 1): S003-S012

[57] Guibert P, Durget M, Murat M (2001) Concentration fields in a confined two-gas mixture and engine in cylinder flow: laser tomography measurements by Mie scattering. Experim. Fluids 31(6): 630-642

[58] Bohren CF, Huffman DR (1983) Absorption and Scattering of Light by Small Particles. John Wiley and Sons, New York

[59] Bevington PR, Robinson DK (2003) Data reduction and error analysis. Vol. 3, McGraw-Hill, New York

[60] Bukai M, Eidelman A, Elperin T, Kleeorin N, Rogachevskii I, Sapir-Katiraie I (2011) Transition phenomena in unstably stratified turbulent flows. Phys. Rev. E 83(3): 036302

[61] Bukai M, Eidelman A, Elperin T, Kleeorin N, Rogachevskii I, Sapir-Katiraie I (2009) Effect of large-scale coherent structures on turbulent convection. Phys. Rev. E 79(6): 066302

[62] Barel L, Eidelman A, Elperin T, Fleurov G, Kleeorin N, Levy A, Rogachevskii I, Shildkrot O (2020) Detection of standing internal gravity waves in experiments with convection over a wavy heated wall. Phys. Fluids 32(9): 095105

[63] Eidelman A, Elperin T, Gluzman I, Kleeorin N, Rogachevskii I (2013) Experimental study of temperature fluctuations in forced stably stratified turbulent flows. Phys. Fluids 25(1): 015111

[64] Cohen N, Eidelman A, Elperin T, Kleeorin N, Rogachevskii I (2014) Sheared stably stratified turbulence and large-scale waves in a lid driven cavity. Phys. Fluids 26(10): 105106.

[65] Eidelman A, Elperin T, Kleeorin N, Hazak G, Rogachevskii I, Sadot O, Sapir-Katiraie I (2009) Mixing at external boundary of submerged turbulent jet. Phys. Rev. E 79(2): 026311

[66] Eidelman A, Elperin T, Kleeorin N, Melnik B, Rogachevskii I (2010) Tangling clustering of inertial particles in stably stratified turbulence. Phys. Rev. E 81(5): 056313

[67] Turner JS (1968) The influence of molecular diffusivity on turbulent entrainment across a density interface. J. Fluid Mech. 33(4): 639-656

[68] Turner JS (1973) Buoyancy Effects in Fluids. Cambridge Univ. Press, Cambridge

[69] Thompson SM, Turner JS (1975) Mixing across an interface due to turbulence generated by an oscillating grid. J. Fluid Mech. 67(2): 349-368

[70] Hopfinger EJ, Toly JA (1976) Spatially decaying turbulence and its relation to mixing across density interfaces. J. Fluid Mech. 78(1): 155-175

[71] Kit E, Strang EJ, Fernando HJS (1997) Measurement of turbulence near shear-free density interfaces. J. Fluid Mech. 334(3): 293-314

[72] Sánchez MA, Redondo JM (1998) Observations from grid stirred turbulence, Appl. Sci. Res. 59(2): 243-254

[73] Medina P, Sánchez MA, Redondo JM (2001), Grid stirred turbulence: applications to the initiation of sediment motion and lift-off studies. Phys. Chem. Earth B 26(4): 299-304